Computers and Fluids 192 (2019) 104273

Contents lists available at ScienceDirect

Computers and Fluids

journal homepage: www.elsevier.com/locate/compfluid

Three dimensional high-order gas-kinetic scheme for supersonic isotropic turbulence I: Criterion for direct numerical simulation

Guiyu Cao[a], Liang Pan[b], Kun Xu[a,c,d,*]

[a] Department of Mathematics, Hong Kong University of Science and Technology, Clear Water Bay, Kowloon, Hong Kong
[b] School of Mathematical Sciences, Beijing Normal University, Beijing, China
[c] Department of Mechanical and Aerospace Engineering, Hong Kong University of Science and Technology, Clear Water Bay, Kowloon, Hong Kong
[d] Shenzhen Research Institute, Hong Kong University of Science and Technology, Shenzhen, China

ARTICLE INFO

Article history:
Received 16 May 2019
Revised 16 August 2019
Accepted 23 August 2019
Available online 23 August 2019

Keywords:
High-order gas-kinetic scheme
Direct numerical simulation
Compressible isotropic turbulence
Supersonic regime.

ABSTRACT

In this paper, we intend to address the high-order gas-kinetic scheme (HGKS) in the direct numerical simulation (DNS) of compressible isotropic turbulence up to the supersonic regime. To validate the performance of HGKS, the compressible isotropic turbulence with initial turbulent Mach number $Ma_{t0} = 0.5$ and Taylor microscale Reynold number $Re_{\lambda 0} = 72$ is simulated as a benchmark. With the consideration of robustness and accuracy, the WENO-Z scheme is adopted for spatial reconstruction in the current higher-order scheme. Statistical quantities are compared with the high-order compact finite difference scheme to determine the spatial and temporal criterion for DNS. According to the grid and time convergence study, it can be concluded that the minimum spatial resolution parameter $\kappa_{\max}\eta_0 \geq 2.71$ and the maximum temporal resolution parameter $\Delta t_{ini}/\tau_0 \leq 27.08/1000$ are adequate for HGKS to resolve the compressible isotropic turbulence, where $\kappa_{\max}$ is the maximum resolved wave number, Δt_{ini} is the initial time step, η_0 and τ_0 are the initial Kolmogorov length scale and time scale, respectively. Guided by such criterion, the compressible isotropic turbulence from subsonic regime $Ma_{t0} = 0.8$ to supersonic one $Ma_{t0} = 1.2$, and the Taylor microscale Reynolds number $Re_{\lambda 0}$ ranging from 10 to 72 are simulated. With the high initial turbulent Mach number, the strong random shocklets and high expansion regions are identified, as well as the wide range of probability density function over local turbulent Mach number. All those impose great challenge for high-order schemes. In order to construct compressible large eddy simulation models at high turbulent Mach number, the ensemble budget of turbulent kinetic energy is fully analyzed. The solenoidal dissipation rate decreases with the increasing of Ma_{t0} and $Re_{\lambda 0}$. Meanwhile, the dilational dissipation rate increases with the increasing of Ma_{t0}, which cannot be neglected for constructing supersonic turbulence model. The current work shows that HGKS provides a valid tool for the numerical and physical studies of isotropic compressible turbulence in supersonic regime, which is much less reported in the current turbulent flow study.

1. Introduction

Compressible turbulence has received great interest for pervading many important engineering applications and natural phenomena, such as hypersonic spacecraft reentry, nuclear fusion power reactors and interstellar turbulence [1]. Isotropic compressible turbulence is regarded as one of cornerstones to elucidate the effects of compressibility for compressible turbulence [2]. Based on the numerical experiments and theoretical analyses, isotropic compressible turbulence is divided into four main dynamical regimes [3], i.e. the low-Mach number quasi-isentropic regime, the low-Mach number thermal regime, the nonlinear subsonic regime, and the supersonic regime. For isotropic incompressible turbulence in periodic box, the pesudo-spectral method (PSM) [4,5] and Lattice-Boltzman method (LBM) [6,7] have been well established and applied for incompressible turbulence. However, both of them are not suitable for compressible turbulence. High-order compact finite difference method (FDM) [8] has been widely utilized in the simulation of isotropic compressible turbulence with moderate turbulent Mach number, ranging from the low-Mach number quasi-isentropic regime to the nonlinear subsonic regime ($Ma_t \leq 0.8$) [9–11]. However, when simulating the turbulent in supersonic regime ($Ma_t \geq 0.8$), it fails to capture strong shocklets and suffers from

* Corresponding author at: Department of Mathematics, Hong Kong University of Science and Technology, Clear Water Bay, Kowloon, Hong Kong.
E-mail addresses: gcaoaa@connect.ust.hk (G. Cao), panliang@bnu.edu.cn (L. Pan), makxu@ust.hk (K. Xu).

https://doi.org/10.1016/j.compfluid.2019.104273
0045-7930/

numerical instability. To study isotropic compressible turbulence with high turbulent Mach number, the piecewise parabolic method (PPM) [12,13] has been applied previously, but the small-scale turbulent structures cannot be resolved due to excessive numerical dissipation. In this decade, aiming at capturing shocklets robustly and resolving smooth region accurately, hybrid scheme combining the compact finite difference scheme and WENO-type scheme has been developed [14,15]. To the authors' knowledge, due to the instability when capturing strong shocklets, the biggest turbulent Mach number of such hybrid scheme [15] has been limited in the critical threshold of supersonic regime, i.e. $Ma_t \approx 1.0$. With a positivity-prerserving reconstruction-failure-detection criterion and a new cooling function, the turbulent Mach number larger than 2.0 could be achieved by the new developed hybrid scheme [16]. For isotropic compressible turbulence in supersonic regime, the stronger random shocklets and higher spatial-temporal gradients pose greater difficulties for numerical analyses than other regimes. Currently, the supersonic regime is much less known and reported, and only a very few systematic numerical experiments are available [17–21].

In the past decades, the gas-kinetic scheme (GKS) based on the Bhatnagar-Gross-Krook (BGK) model [22,23] has been developed systematically for the computations from low speed flow to supersonic one [24–26]. Different from the numerical methods based on the macroscopic governing equations, the gas-kinetic scheme presents a gas evolution process from kinetic scale to hydrodynamic scale, where both inviscid and viscous fluxes are recovered from the moments of a single time-dependent gas distribution function [25,26]. In discontinuous shock region, the kinetic scale physics takes effect to construct a crisp and stable shock transition. In smooth flow region, the hydrodynamic scale physics corresponding to the multi-dimensional central difference discretization will contribute mainly in the kinetic flux function, and accurate Navier-Stokes solution can be obtained once the flow structure is well resolved. Both normal and tangential gradients of flow variables are included in the flux function across a cell interface [27,28]. With the two-stage temporal discretization for the Lax-Wendroff type flow solvers [29–31], a reliable framework was provided for developing the GKS into fourth-order and even higher-order accuracy with the implementation of the traditional second-order or third-order flux functions [32,33]. More importantly, this scheme is as robust as the second-order scheme and works perfectly from the subsonic to the hypersonic viscous heat conducting flows [34]. In comparison with Riemann solver based CFD methods, the robustness is solely due to the dynamical evolution model of the time dependent flux function. For the higher-order schemes, it seems that a reliable physical evolution model becomes more important due to the absence of large numerical dissipation in the second-order schemes, and the delicate flow structures captured in higher-order schemes depend on the quality of the solvers greatly [33]. In recent years, GKS has been applied in turbulence simulation successfully. For high-Reynolds number turbulent flows, the second-order and third-order GKS coupled with traditional eddy-viscosity turbulence models [35–38] have been developed and implemented in turbulent flow simulations, where a newly turbulent collision time τ_t was defined to model the turbulent behavior on unresolved grids. As for low-Reynolds number turbulent flows, the GKS based on modified WENO reconstruction [39,40] have been implemented in direct numerical simulation (DNS) of decaying isotropic compressible turbulence. Numerical results confirm the great advantage of GKS in high-speed flow simulation. Recently, with the two-stage temporal discretization and WENO reconstruction [41–43], the high-order GKS (HGKS) is constructed for simulating three-dimensional flows [44]. Numerical results show the capability to simulate the complicated flows, such as the isotropic compressible turbulence.

In this paper, we concentrate on the DNS of compressible isotropic turbulence with high turbulent Mach number, and the two-stage fourth-order gas-kinetic scheme [30] is adopted to simulate the compressible isotropic turbulence up to supersonic regime. In the previous studies, the high resolution can be obtained only in space. However, high-order accuracy in time is also necessarily required for DNS to fully resolve the smallest eddies in turbulent flows, i.e. the eddies in Kolmogorov length scale and time scale. As a first attempt, the validation of fourth-order GKS for compressible isotropic turbulence is undertaken to obtain the criterion to guide the subsequent studies. The current study indicates that the minimum spatial resolution parameter $\kappa_{\max}\eta_0 \geq 2.71$ and the maximum temporal resolution parameter $\Delta t_{ini}/\tau_0 \leq 27.08/1000$ are adequate for the HGKS to resolve the isotropic compressible turbulence. With the increasing of initial turbulent Mach number, the range of the probability density function (PDF) over local turbulent Mach number becomes wide at the same fixed normalized time. In addition, stronger random shocklets and higher expansion regions are observed with the higher initial turbulent Mach number, which exert great difficulties for high-order schemes. Statistical quantities are presented for these cases, which are used as the benchmark for supersonic isotropic turbulence. The solenoidal dissipation rate is lower with the higher Ma_{t0} and $Re_{\lambda 0}$. At the same time, it is observed that the dilational dissipation rate increases with the increasing of Ma_{t0}, and seems slightly dependent on $Re_{\lambda 0}$. This analysis lays foundation for constructing compressible large eddy simulation (LES) in supersonic regime. This study confirms that HGKS provides a valid tool for the studies of complex compressible turbulent flows.

This paper is organized as follows. In Section 2, a brief review on the fourth-order GKS will be presented. Section 3 presents the detailed flow conditions and statistical turbulence quantities for isotropic compressible turbulence. Numerical validation and discussions will be presented in Section 4. Conclusions are shown in the final section.

2. Two-stage fourth-order gas-kinetic scheme

The three-dimensional BGK equation [22,23] can be written as

$$f_t + uf_x + vf_y + wf_z = \frac{g-f}{\tau}, \tag{1}$$

where (u, v, w) is the particle velocity, f is the gas distribution function, g is the three-dimensional Maxwellian distribution, and τ is the collision time. The collision term satisfies the compatibility condition

$$\int \frac{g-f}{\tau}\psi \,\mathrm{d}\Xi = 0, \tag{2}$$

where $\psi = (\psi_1, \ldots, \psi_5)^T = (1, u, v, w, \frac{1}{2}(u^2+v^2+w^2+\xi^2))^T$, the internal variables ξ^2 equals to $\xi^2 = \xi_1^2 + \ldots + \xi_K^2$, $\mathrm{d}\Xi = \mathrm{d}u\mathrm{d}v\mathrm{d}w\mathrm{d}\xi^1 \ldots \mathrm{d}\xi^K$, K is the degrees of freedom, and the specific heat ratio $\gamma = (K+5)/(K+3)$ for three-dimensional flows. Based on the Chapman–Enskog expansion, the Euler and Navier–Stokes equations can be derived [25,26].

Taking conservative moments of Eq. (1) and integrating over the control volume $V_{ijk} = \bar{x}_i \times \bar{y}_j \times \bar{z}_k$ with $\bar{x}_i = [x_i - \Delta x/2, x_i + \Delta x/2], \bar{y}_j = [y_j - \Delta y/2, y_j + \Delta y/2], \bar{z}_k = [z_k - \Delta z/2, z_k + \Delta z/2]$, the semi-discretized finite volume scheme can be written as

$$\begin{aligned}\frac{\mathrm{d}Q_{ijk}}{\mathrm{d}t} = \mathcal{L}(Q_{ijk}) = \frac{1}{\Delta x\Delta y\Delta z}\Big[&\int_{\bar{y}_j\times\bar{z}_k}(F_{i-1/2,j,k} - F_{i+1/2,j,k})\mathrm{d}y\mathrm{d}z \\ &+ \int_{\bar{x}_i\times\bar{z}_k}(G_{i,j-1/2,k} - G_{i,j+1/2,k})\mathrm{d}x\mathrm{d}z \\ &+ \int_{\bar{x}_i\times\bar{y}_j}(H_{i,j,k-1/2} - H_{i,j,k+1/2})\mathrm{d}x\mathrm{d}y\Big],\end{aligned} \tag{3}$$

where $Q = (\rho, \rho U, \rho V, \rho W, \rho E)^T$ are the conservative flow variables, Q_{ijk} is the cell averaged value over the control volume V_{ijk}. For the direct numerical simulation of the compressible isotropic turbulence, the semi-discretized finite volume scheme Eq. (3) needs to be fully discretized with high-order accuracy. Recently, a two-stage fourth-order time-accurate discretization has been developed for Lax-Wendroff type flow solvers [29,30], which provides a reliable framework to develop high-order scheme for three-dimensional flows with complicated flow structure. Consider the following time-dependent equation

$$\frac{dQ}{dt} = \mathcal{L}(Q),$$

with initial condition

$$Q(t = t_n) = Q^n,$$

where $\mathcal{L}$ is an operator for spatial derivative of flux given by Eq. (3), and the subscript of Q_{ijk} is omitted for simplicity. The state Q^{n+1} is updated with the following formula

$$\begin{aligned} Q^* &= Q^n + \frac{1}{2}\Delta t \mathcal{L}(Q^n) + \frac{1}{8}\Delta t^2 \frac{\partial}{\partial t}\mathcal{L}(Q^n), \; Q^{n+1} = Q^n + \Delta t \mathcal{L}(Q^n) \\ &+ \frac{1}{6}\Delta t^2\Big(\frac{\partial}{\partial t}\mathcal{L}(Q^n) + 2\frac{\partial}{\partial t}\mathcal{L}(Q^*)\Big). \end{aligned} \tag{4}$$

It can be proved that for hyperbolic equations the above time stepping method Eq. (4) provides a fourth-order time accurate solution for $Q(t)$ at $t = t_n + \Delta t$ [29,30].

To achieve the high-order spatial accuracy, the Gaussian quadrature for the numerical flux is used at the cell interface. For example, the numerical flux in x-direction is given as

$$\int_{\bar{y}_j \times \bar{z}_k} F_{i+1/2,j,k} dy dz = \Delta y \Delta z \sum_{m,n=1}^{2} \omega_{mn} F(\boldsymbol{x}_{i+1/2,j_m,k_n}, t), \tag{5}$$

where ω_{mn} is the quadrature weight, $\boldsymbol{x}_{i+1/2,m,n} = (x_{i+1/2}, y_{j_m}, z_{k_n})$, (y_{j_m}, z_{k_n}) is the Gauss quadrature point of the cell interface $\bar{y}_j \times \bar{z}_k$, and the numerical flux $F(\boldsymbol{x}_{i+1/2,j_m,k_n}, t)$ is provided by taking moments of the gas distribution function

$$F(\boldsymbol{x}_{i+1/2,j_m,k_n}, t) = \int \psi u f(\boldsymbol{x}_{i+1/2,j_m,k_n}, t, \boldsymbol{u}, \xi) du dv dw d\xi. \tag{6}$$

For the three-dimensional flows, the gas distribution function at the Gauss quadrature point is given by the second-order gas-kinetic solver as follows

$$\begin{aligned} f(\boldsymbol{x}_{i+1/2,j_m,k_n}, t, \boldsymbol{u}, \xi) &= (1 - e^{-t/\tau})g_0 + ((t+\tau)e^{-t/\tau} - \tau) \\ &\times (\bar{a}_1 u + \bar{a}_2 v + \bar{a}_3 w)g_0 + (t - \tau + \tau e^{-t/\tau})\bar{A}g_0 \\ &+ e^{-t/\tau} g_r[1 - (\tau + t)(a_{1r}u + a_{2r}v + a_{3r}w) - \tau A_r)]H(u) \\ &+ e^{-t/\tau} g_l[1 - (\tau + t)(a_{1l}u + a_{2l}v + a_{3l}w) - \tau A_l)](1 - H(u)). \end{aligned}$$

In order to implement the two-stage method, Eq. (6) is approximated by a linear function

$$F(\boldsymbol{x}_{i+1/2,j_m,k_n}, t) \approx \underbrace{F_{i+1/2,j,k}(Q^n, t_n)}_{\mathcal{L}} + \underbrace{\partial_t F_{i+1/2,j,k}(Q^n, t_n)}_{\mathcal{L}_t} t.$$

More details for the implementation of gas-kinetic scheme can be found in the literature [30,32].

To achieve the high-order spatial accuracy, the fifth-order WENO reconstruction [41–43] is adopted at the Gaussian quadrature points. The one-dimensional WENO scheme is given as follows

$$Q_i^r = \sum_{k=0}^{2} \omega_k Q_i^{kr}, \quad Q_i^l = \sum_{k=0}^{2} \tilde{\omega}_k Q_i^{kl},$$

where Q_i^{kr} and Q_i^{kl} are obtained by the third-order interpolation, and ω_k is the nonlinear weight. The nonlinear weights of WENO-JS [42] and WENO-Z [43] scheme are given as follows

$$\omega_k^{JS} = \frac{\alpha_k^{JS}}{\sum_{m=0}^{2} \alpha_m^{JS}}, \quad \alpha_k^{JS} = \frac{d_k}{\beta_k + \varepsilon}, \quad \omega_k^{Z} = \frac{\alpha_k^{Z}}{\sum_{m=0}^{2} \alpha_m^{Z}},$$
$$\alpha_k^{Z} = d_k\Big[1 + \Big(\frac{\tau}{\beta_k + \varepsilon}\Big)\Big],$$

where d_k is the linear weight

$$d_0 = \frac{3}{10}, d_1 = \frac{3}{5}, d_2 = \frac{1}{10},$$

β_k is the smooth indicator for each candidate stencil

$$\beta_0 = \frac{13}{12}(Q_i - 2Q_{i+1} + Q_{i+2})^2 + \frac{1}{4}(3Q_i - 4Q_{i+1} + Q_{i+2})^2,$$
$$\beta_1 = \frac{13}{12}(Q_{i-1} - 2Q_i + Q_{i+1})^2 + \frac{1}{4}(Q_{i-1} - Q_{i+1})^2,$$
$$\beta_2 = \frac{13}{12}(Q_{i-2} - 2Q_{i-1} + Q_i)^2 + \frac{1}{4}(Q_{i-2} - 4Q_{i-1} + Q_i)^2,$$

$\epsilon = 10^{-6}$ and $\tau = |\beta_0 - \beta_2|$ is used for WENO-Z scheme.

In the high-order gas-kinetic scheme, the conservative variables Q_0 can be determined according to the compatibility condition Eq. (2)

$$\int \psi g_0 d\Xi = Q_0 = \int_{u>0} \psi g_l d\Xi + \int_{u<0} \psi g_r d\Xi.$$

where g_l and g_r are the equilibrium states corresponding to the conservative variables Q_i^r and Q_{i+1}^l at the cell interface. With the reconstructed variables, the normal spatial derivatives for the conservative variables at left side, right side and across the cell interface can be given as follows

$$\partial_x Q_l = (Q_i^r - Q_i^l)/\Delta x, \;\; \partial_x Q_r = (Q_{i+1}^r - Q_{i+1}^l)/\Delta x,$$
$$\partial_x Q_0 = \Big[-\frac{1}{12}(Q_{i+2} - Q_{i-1}) + \frac{5}{4}(Q_{i+1} - Q_i)\Big]/\Delta x.$$

With the reconstructed conservative variables and normal derivatives in normal direction, the point value Q_l, Q_r and Q_0 and first-order derivatives at the Gauss quadrature points $\boldsymbol{x}_{i+1/2,m,n} = (x_{i+1/2}, y_{j_m}, z_{k_n})$ can be constructed. The detailed procedure is given as follows

1. According to one dimensional reconstruction, the cell averaged reconstructed values and cell averaged spatial derivatives

   $(Q_l)_{j-\ell_1,k-\ell_2}, (Q_r)_{j-\ell_1,k-\ell_2}, (Q_0)_{j-\ell_1,k-\ell_2},$
   $(\partial_x Q_l)_{j-\ell_1,k-\ell_2}, (\partial_x Q_r)_{j-\ell_1,k-\ell_2}, (\partial_x Q_0)_{j-\ell_1,k-\ell_2},$

   can be constructed, where $\ell_1, \ell_2 = -2, \ldots, 2$.
2. With the one-dimensional WENO reconstruction in the horizontal direction, the averaged value and the averaged spatial derivatives

   $(Q_l)_{j_m,k-\ell_2}, (Q_r)_{j_m,k-\ell_2}, (Q_0)_{j_m,k-\ell_2},$
   $(\partial_x Q_l)_{j_m,k-\ell_2}, (\partial_x Q_r)_{j_m,k-\ell_2}, (\partial_x Q_0)_{j_m,k-\ell_2},$
   $(\partial_y Q_l)_{j_m,k-\ell_2}, (\partial_y Q_r)_{j_m,k-\ell_2}, (\partial_y Q_0)_{j_m,k-\ell_2}$

   over the interval $[z_{k-\ell_2} - \Delta z/2, z_{k-\ell_2} + \Delta z/2]$ with $y = y_{j_m}$ can be given.
3. With one-dimensional WENO reconstruction in the vertical direction, the point value and spatial derivatives

   $(Q_l)_{j_m,k_n}, (Q_r)_{j_m,k_n}, (Q_0)_{j_m,k_n},$
   $(\partial_x Q_l)_{j_m,k_n}, (\partial_x Q_r)_{j_m,k_n}, (\partial_x Q_0)_{j_m,k_n},$
   $(\partial_y Q_l)_{j_m,k_n}, (\partial_y Q_r)_{j_m,k_n}, (\partial_y Q_0)_{j_m,k_n},$
   $(\partial_z Q_l)_{j_m,k_n}, (\partial_z Q_r)_{j_m,k_n}, (\partial_z Q_0)_{j_m,k_n},$

can be fully determined at the Gaussian quadrature points $\boldsymbol{x}_{i+1/2,m,n} = (x_{i+1/2}, y_{j_m}, z_{k_n})$.

Remark: For the tangential reconstruction of Q_0, the fourth-order polynomials are constructed at the horizontal and vertical direction. The variables and spatial derivatives can be constructed at the Guassian quadrature points.

For the tangential reconstruction of $Q_{l,r}$, the variables at the ends of cell interface can be obtained from the fifth-order WENO method at the horizontal and vertical direction. With reconstructed variables and the cell averaged variables, the quadratic polynomials can be constructed. The variables and spatial derivatives can be constructed at the Guassian quadrature points as well.

In the part of code validation, the smooth flow fields without strong shocklets at $Ma_{t0} = 0.1, 0.3$ and 0.5 are calculated first. The simplified smooth second-order gas-kinetic flux [44] and WENO scheme with linear weights (WENO-L) are used in the validation. To improve the robustness without losing too much accuracy, for the isotropic turbulence from subsonic to supersonic regime, i.e. $Ma_{t0} \geq 0.5$, the variable Q_0 takes the identical tangential reconstruction of $Q_{l,r}$ in WENO-JS [42] and WENO-Z [43] scheme.

More details of three-dimensional high-order gas-kinetic scheme can be found in the reference [44].

3. Decaying isotropic compressible turbulence

The isotropic compressible turbulence is regarded as one of fundamental benchmarks to study the compressible effect. Both forced isotropic compressible turbulence with solenoidal and dilational external force [11,45,46] and decaying isotropic compressible turbulence [5,9,10] are studied in the literature. In this paper, we concentrate on the decaying isotropic compressible turbulence without external force. The flow domain of numerical simulation is a cube box defined as $[-\pi, \pi] \times [-\pi, \pi] \times [-\pi, \pi]$, with periodic boundary conditions in all three Cartesian directions for all the flow variables. Evolution of this artificial system is determined by initial thermodynamic quantities and two dimensionless parameters, i.e. the initial Taylor microscale Reynolds number

$$Re_\lambda = \frac{\langle \rho \rangle u_{rms} \lambda_t}{\langle \mu \rangle},$$

and turbulent Mach number

$$Ma_t = \frac{\sqrt{3} u_{rms}}{\langle c_s \rangle},$$

where $\langle \cdot \rangle$ is the ensemble over the whole computational domain, ρ is the density, λ_t is the Taylor microscale, μ is the initial dynamic viscosity, c_s is the sound speed and u_{rms} is the root mean square of initial turbulent velocity component

$$u_{rms} = \left\langle \frac{\boldsymbol{u} \cdot \boldsymbol{u}}{3} \right\rangle^{1/2}.$$

A three-dimensional solenoidal random initial velocity field $\boldsymbol{u}$ can be generated by a specified spectrum, which is given by [47]

$$E(\kappa) = A_0 \kappa^4 \exp(-2\kappa^2/\kappa_0^2), \tag{7}$$

where A_0 is a constant to get a specified initial kinetic energy, κ is the wave number, κ_0 is the wave number at which the spectrum peaks. In this paper, fixed A_0 and κ_0 in Eq. (7) are chosen for all cases, which are initialized by $A_0 = 0.00013$ and $\kappa_0 = 8$. Initial strategies play an important role in isotropic compressible turbulence simulation [9], especially for the starting fast transient period during which the divergence of the velocity increases rapidly and the negative temperature or pressure often appear. In the computation, the initial pressure p_0, density ρ_0 and temperature T_0 are set as constant. In this way, the initial Taylor microscale Reynolds number $Re_{\lambda 0}$ and turbulent Mach number Ma_{t0} can be determined by

$$Re_{\lambda 0} = \frac{(2\pi)^{1/4}}{4} \frac{\rho_0}{\mu_0} \sqrt{2A_0} \kappa_0^{3/2},$$

$$Ma_{t0} = \frac{\sqrt{3}}{\sqrt{\gamma R T_0}} u_{rms},$$

where the initial density $\rho_0 = 1$, μ_0, T_0 can be determined by $Re_{\lambda 0}$ and Ma_{t0} and $\gamma = 1.4$ is the specific heat ratio. In the simulation, the dynamic velocity is given by

$$\mu = \mu_0 (\frac{T}{T_0})^{0.76}. \tag{8}$$

With current initial strategy, the initial ensemble turbulent kinetic energy K_0, ensemble enstrophy Ω_0, ensemble dissipation rate ε_0, large-eddy-turnover time τ_{to}, Kolmogorov length scale η_0, and the Kolmogorov time scale τ_0 are given as

$$K_0 = \frac{3A_0}{64} \sqrt{2\pi} \kappa_0^5, \quad \Omega_0 = \frac{15A_0}{256} \sqrt{2\pi} \kappa_0^7, \quad \tau_{to} = \sqrt{\frac{32}{A_0}} (2\pi)^{1/4} \kappa_0^{-7/2},$$

$$\varepsilon_0 = 2\frac{\mu_0}{\rho_0} \Omega_0, \quad \eta_0 = (\nu_0^3/\varepsilon_0)^{1/4}, \quad \tau_0 = (\nu_0/\varepsilon_0)^{1/2}. \tag{9}$$

For decaying compressible isotropic turbulence, the local turbulent Mach number M_{loc}, root-mean-square density fluctuations ρ_{rms}, and turbulent kinetic energy K are defined as

$$M_{loc} = \frac{\sqrt{\boldsymbol{u} \cdot \boldsymbol{u}}}{c_{loc}},$$

$$\rho_{rms} = \sqrt{\langle \rho - \langle \rho \rangle \rangle},$$

$$K = \frac{1}{2} \langle \rho \boldsymbol{u} \cdot \boldsymbol{u} \rangle, \tag{10}$$

where c_{loc} is the local sound speed. Starting from the initial flows, the large eddies transfer their turbulent kinetic energy successively to smaller eddies. In this process, the evolution of turbulent kinetic energy is of interest since it is a fundamental benchmark for incompressible and compressible turbulence modeling [48–50]. In this study, the ensemble budget of turbulent kinetic energy is computed and analyzed, as the decay of the ensemble turbulent kinetic energy can be described approximately by Sarkar et al. [51]

$$\frac{\mathrm{d}\langle K \rangle}{\mathrm{d}t} = \varepsilon + \langle p\theta \rangle,$$

$$\varepsilon = \varepsilon_s + \varepsilon_d, \tag{11}$$

where $\varepsilon_s = \langle \mu \omega_i \omega_i \rangle$ is the ensemble solenoidal dissipation rate, $\varepsilon_d = \langle \frac{4}{3} \mu \theta^2 \rangle$ is the ensemble dilational dissipation rate, $\langle p\theta \rangle$ is the ensemble pressure-dilation transfer, $\omega_i = \epsilon_{ijk} \frac{\partial u_k}{\partial x_j}$ is the fluctuating vorticity, ϵ_{ijk} is the alternating tensor and $\theta = \nabla \cdot \boldsymbol{u}$ is the fluctuating divergence of velocity.

4. Numerical simulation and discussions

In this section, numerical simulation and discussions for isotropic compressible turbulence will be presented. In all simulations, the collision time τ takes

$$\tau = \frac{\mu}{p} + C \frac{|p_L - p_R|}{|p_L + p_R|} \Delta t,$$

where μ is the viscous coefficient obtained from Eq. (8), p_L and p_R denote the pressures on the left and right hand sides at the cell interface. The collision time reduces to $\tau = \mu/p$ in the smooth flow region. The constant C takes 1.5 in the computation, and Δt is the time step determined according to the CFL condition.

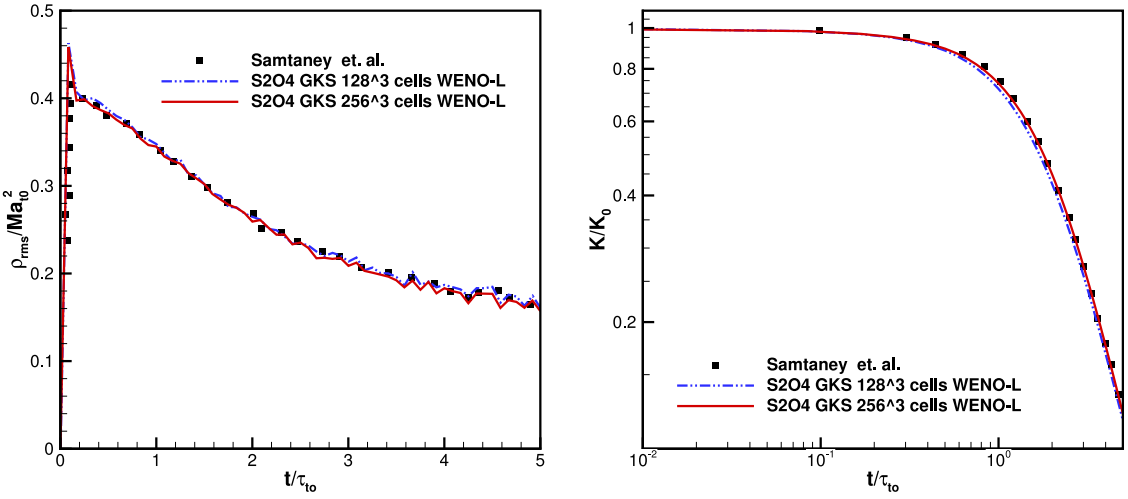

Fig. 1. Time history of ρ_{rms}/Ma_{t0}^2 and K/K_0 for the near incompressible isotropic turbulence with $Re_{\lambda 0} = 72$ and $Ma_{t0} = 0.1$.

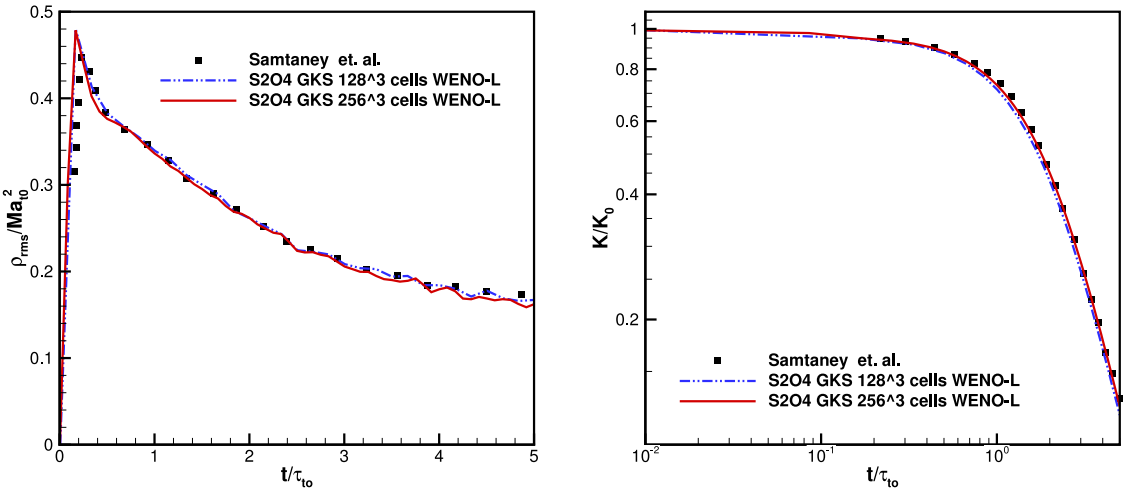

Fig. 2. Time history of ρ_{rms}/Ma_{t0}^2 and K/K_0 for the isotropic compressible turbulence in nonlinear subsonic regime with $Re_{\lambda 0} = 72$ and $Ma_{t0} = 0.3$.

4.1. Code validation

To validate performance of HGKS, the near incompressible isotropic turbulence with $Ma_{t0} = 0.1$ and the compressible isotropic turbulence in nonlinear subsonic regime with $Ma_{t0} = 0.3$ are tested firstly. In these two cases with low turbulent Mach number, the flow fields are smooth without strong shocklets. To improve the resolution of simulation, the WENO scheme with linear weights denoted as WENO-L is adopted. The uniform grids with 128^3 and 256^3 cells are used. The time history of normalized root-mean-square density fluctuation ρ_{rms}/Ma_{t0}^2 and normalized turbulent kinetic energy K/K_0 with respect to t/τ_{to} are given in Figs. 1 and 2. For these isotropic turbulent flows with low turbulent Mach number, the WENO-L can well resolve the flow structures. Numerical results of current scheme agree well with the reference data in [9]. Because of the lower dissipation of WENO-L scheme, the convergent solutions can be provided by a uniform 128^3 grid points.

However, with the increase of turbulent Mach number, the eddy-shocklets appear in the flow fields and the WENO-L scheme blows up at $Ma_{t0} > 0.5$. Hence, the WENO scheme with nonlinear weights have to be used to capture the discontinuities when simulating high turbulent Mach number flows. Before we study the compressible isotropic turbulence in supersonic regime, it is legitimate to study the behavior of high-order GKS with different WENO schemes. The decaying isotropic compressible turbulence with $Re_{\lambda 0} = 72$ and $Ma_{t0} = 0.5$ is used to test the performance of three widely used WENO schemes, i.e. WENO-L, WENO-JS and WENO-Z schemes. The uniform grids with 128^3 and 256^3 cells are used as well. The time history of normalized root-mean-square density fluctuation ρ_{rms}/Ma_{t0}^2 and normalized turbulent kinetic energy K/K_0 with respect to t/τ_{to} for three WENO schemes are given in Fig. 3. The convergent solutions can be provided by the WENO-L scheme with 128^3 uniform grids, while WENO-JS scheme and WENO-Z scheme are more dissipative than WENO-L scheme. More specifically, the WENO-JS is more dissipative than WENO-Z scheme. According to the following numerical tests ($Ma_{t0} \geq 0.5$), the WENO-Z is almost as robust as WENO-JS for the isotropic compressible turbulence. Considering the robustness and dissipative behavior, the WENO-Z scheme will be used in the following simulations.

The time convergence is studied as well and the same isotropic compressible turbulence at $Re_{\lambda 0} = 72$ and $Ma_{t0} = 0.5$ is used. In order to resolve and capture the desired physics in the high turbulent Mach number regime, several strategies for the choice of time step are provided in previous studies. Time step is set as $\tau_{to}/1000$ [15] in hybrid scheme, which is very expansive when implementing DNS on isotropic compressible turbulence even with moderate Taylor microscale Reynolds number. In the DNS using high-resolution modified-WENO GKS [40], the maximum CFL number can get up to 0.8. Thus, study of the criterion for time step of cur-

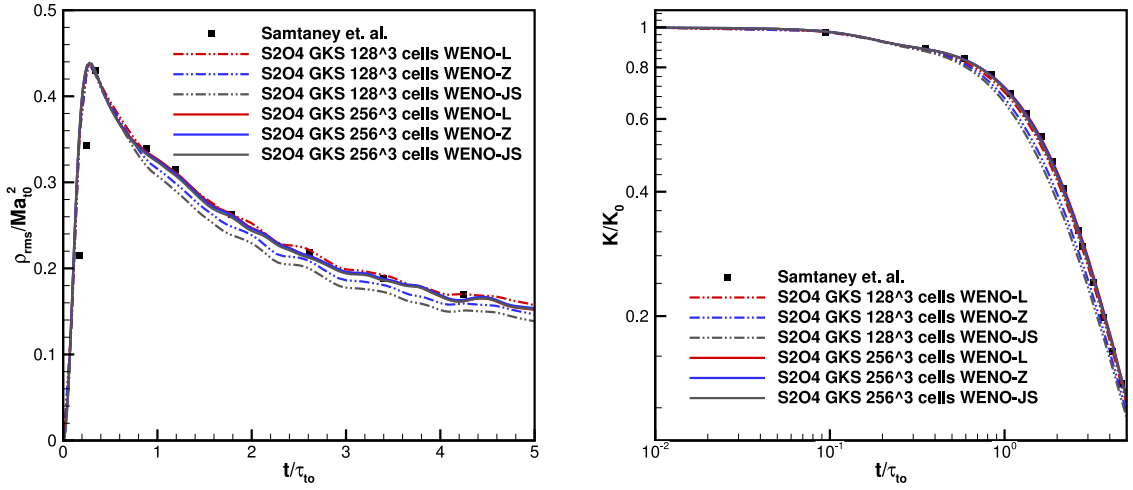

Fig. 3. Time history of ρ_{rms}/Ma_{t0}^2 and K/K_0 for the isotropic compressible turbulence with $Re_{\lambda 0} = 72$ and $Ma_{t0} = 0.5$ for WENO-L, WENO-JS and WENO-Z schemes.

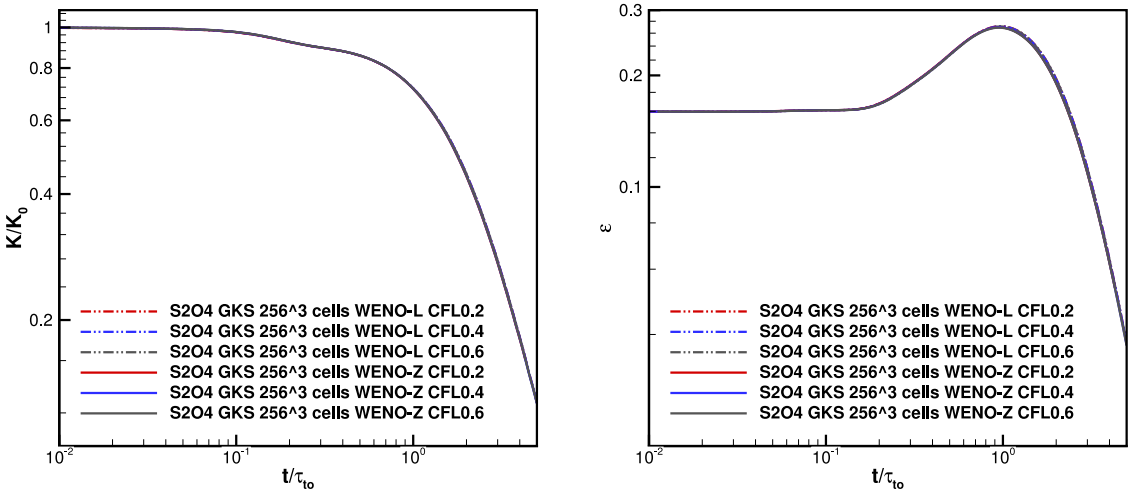

Fig. 4. Time convergence study: Time history of K/K_0 and ε for the isotropic compressible turbulence with $Re_{\lambda 0} = 72$ and $Ma_{t0} = 0.5$ with CFL number 0.2, 0.4 and 0.6.

Table 1
Different CFL number for time convergence study.

CFL number	dt_{ini}/τ_0	dt_{end}/τ_0	dt_{ini}/τ_{to}	dt_{end}/τ_{to}
0.2	9.02/1000	14.00/1000	1.86/1000	2.89/1000
0.4	18.05/1000	28.03/1000	3.72/1000	5.78/1000
0.6	27.08/1000	42.06/1000	5.58/1000	8.66/1000

Table 2
Grid size and characteristic length scales for grid convergence study.

Grid size	Δ/λ_0	Δ/η_0	$\kappa_{\max}\eta_0$
256^3	8.162	1.639	1.806
384^3	5.441	1.093	2.710
512^3	4.081	0.819	3.613

rent fourth-order GKS is required. Time convergence study with different CFL number are presented in Table 1, where dt_{ini} and dt_{end} represent the time step for the initial step and ending step, respectively. In this simulation, the ending step is defined at the moment of $t/\tau_{to} = 5$. The time history of normalized K/K_0 and the ensemble total dissipation rate ε with CFL number $CFL = 0.2, 0.4$ and 0.6 on uniform grids with 256^3 cells are shown in Fig 4. In current paper, the velocity gradients for Eq. (11) are computed by first-order upwind scheme. As the consistent results are obtained using different CFL number with WENO-L and WENO-Z schemes, time convergent solution can be obtained with CFL number $CFL = 0.6$, which is in agreement with modified-WENO GKS [40]. For this case, the initial Kolmogorov time scale τ_0 and the initial large-eddy turnover time τ_{to} can be determined by Eq. (9). According to Table. 1, the time step can be set as large as $t_{ini}/\tau_{to} = 5.58/1000$. Meanwhile, the time step can well resolve the smallest timescale as $t_{ini}/\tau_0 = 27.08/1000$.

Grid convergence study is also required [15,52] to conclude the criterion for space resolution when using the fourth-order GKS as a DNS tool. Three different uniform grids with 256^3, 384^3 and 512^3 cells and characteristic length scales are demonstrated in Table 2, where λ_0 is the initial mean free path approximated by $\mu_0 = 1/3\rho_0 c_0 \lambda_0$ [26], Δ is the uniform grid size in each direction, η_0 is the initial Kolmogorov length scale as in Eq. (9), $\kappa_{\max} = \sqrt{2}\kappa_0 N/3$ is the maximum resolved number wave number [53], $\kappa_0 = 8$ as Eq. (7) and N is the number of grid points in each Cartesian direction. According to Table 2, the Kolmogorov length scale is almost 5 times larger than the mean free path, and each grid always contains several mean free path even for the finest grids with 512^3 cells. This provides the intuitive evidence for controversial issue that smallest eddies in turbulence may still within the framework of continuum mechanics assumption. The behavior of normalized ρ_{rms}/Ma_{t0}^2, K/K_0 and turbulent kinetic energy budget

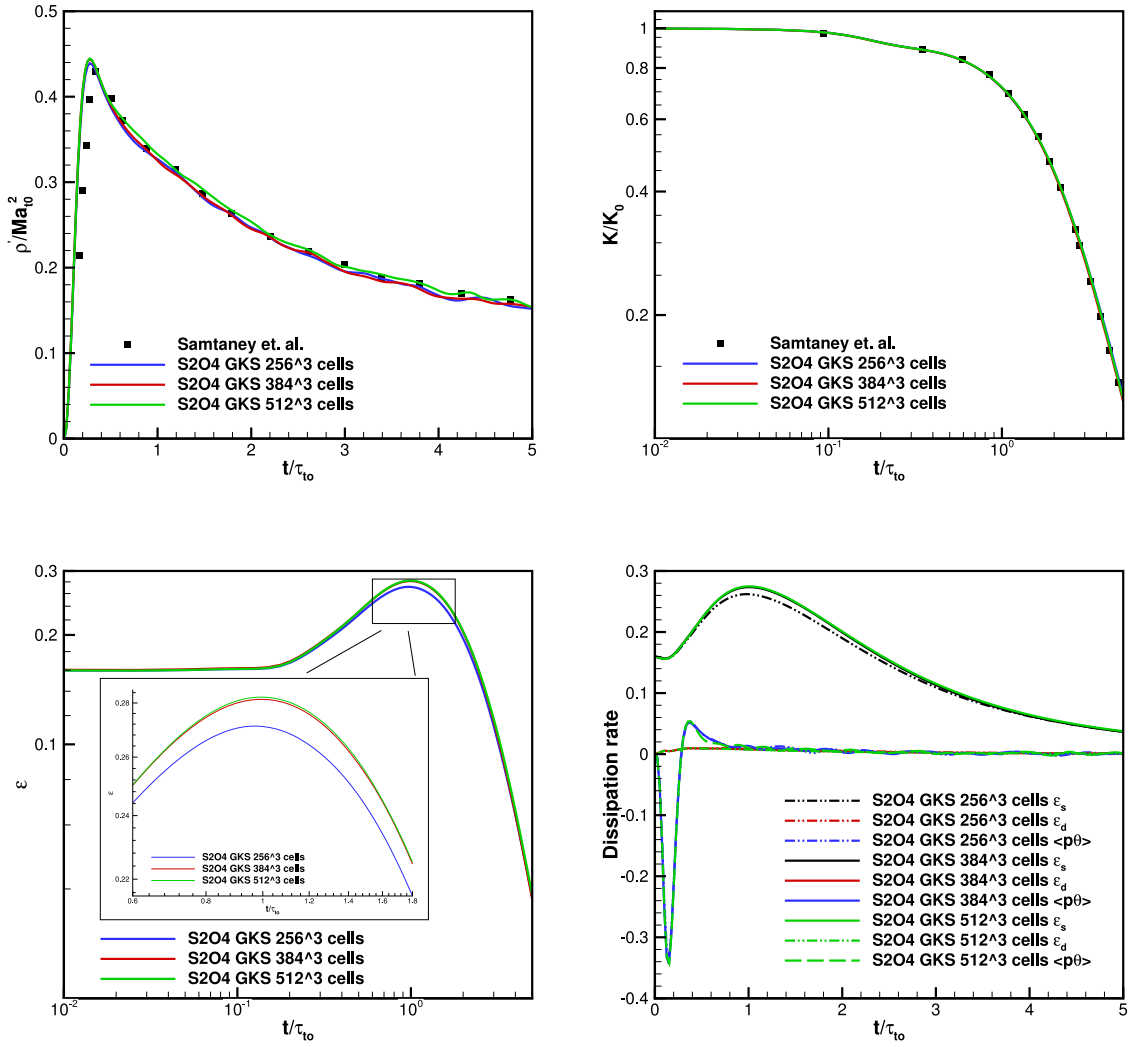

Fig. 5. Grid convergence study: Time history of ρ_{rms}/Ma_{t0}^2, K/K_0, ε, ε_d, ε_s and $\langle p\theta \rangle$ for isotropic compressible turbulent with $Re_{\lambda 0} = 72$ and $Ma_{t0} = 0.5$ on uniform grids with 256^3, 384^3 and 512^3 cells.

defined in Eq. (11) are presented in Fig 5. The key statistical quantities on uniform grids with 384^3 cells coincide with those on uniform grids with 512^3 cells. It can be concluded that the minimum spatial resolution parameter $\kappa_{\max}\eta_0 \geq 2.71$ is adequate for resolving the isotropic compressible turbulence of HGKS. This criterion is similar to that in the hybrid scheme [15], which has been applied in isotropic compressible turbulence successfully. According to the simulations above, the criterion of spatial and temporal resolution for fourth-order GKS based on WENO-Z reconstruction is obtained, namely, the spatial resolution parameter $\kappa_{\max}\eta_0 \geq 2.71$ and the temporal resolution parameter $\Delta t_{ini}/\tau_0 \leq 27.08/1000$.

Iso-surface of the second invariant of velocity gradient tensor $Q = 25$ and PDF of dilation θ for uniform grids with 384^3 cells at $t/\tau_{to} = 0.5$ are shown in Fig 6. Iso-surface is colored by local turbulent Mach number in a 128^3 sub-domain covering $(105\eta_0)^3$ (1/27 of the whole domain), where the sub-domain is located at the center of the full domain. The local turbulent Mach number concentrates on the near region of $Ma_t = 0.4$, which is much smaller than the latter simulation with high turbulent Mach numbers. All PDFs of dilation in this paper are obtained by dividing the dilation range into 1000 equivalent intervals, the velocity gradients for local dilation value θ are computed by the second-order central difference. At the initial stage, the symmetric dilation range is $[-1.08, 1.08]$, while the skewed dilation range with minimum and maximum values -105.8 and 23.9 at $t/\tau_{to} = 0.5$ appears. This quite wide range of dilation is an intrinsic property for isotropic compressible turbulence which means the strong compression and expansion regions exist in the flow field.

4.2. Turbulent mach number effect

In this section, DNS of isotropic compressible turbulence from high subsonic regime to supersonic regime with moderate Taylor microscale Reynolds number are tested. The effect of compressibility on dynamics and structures of isotropic compressible turbulence in moderate subsonic regime ($Ma_t \leq 0.8$) has been studied previously [10,51]. The statistical properties and dynamics of forced supersonic regime $Ma_t \approx 1.0$ have been studied systematically [17–19,55]. The numerical tests $R1 - R5$ given in Table. 3 go beyond previous study up to the maximum supersonic turbulent Mach number $Ma_{t0} = 1.2$ with a fixed initial Taylor microscale Reynolds number $Re_{\lambda 0} = 72$. In the computation, a uniform grids with 384^3 cells are used and $\kappa_{\max}\eta_0 = 2.71$. As shown in Fig. 7, the PDF of initial local turbulent Mach number deviates from symmetric distribution and the maximum local turbulent Mach number for R_1, R_3 and R_5 can be three times higher than ensemble initial turbulent Mach number Ma_{t_0}. For this decaying isotropic compressible turbulence, the ensemble turbulent Mach number becomes

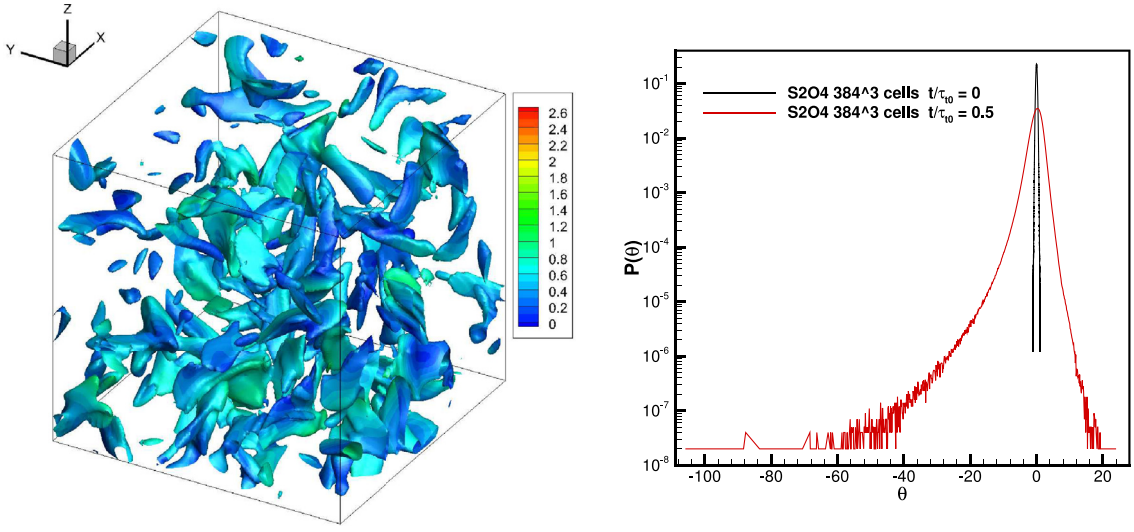

Fig. 6. Iso-surface of the second invariant of velocity gradient tensor $Q = 25$ and PDF of dilation θ with $Re_{\lambda 0} = 72$ and $Ma_{t0} = 0.5$ on uniform grids with 384^3 cells at $t/\tau_{to} = 0.5$.

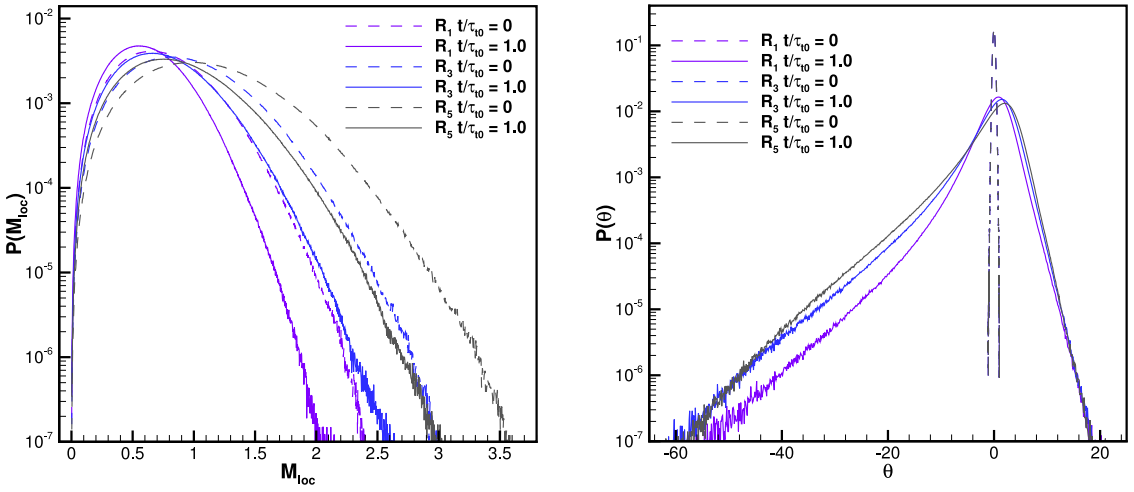

Fig. 7. PDF of local turbulent Mach number and root-mean-square dilation at $t/\tau_{to} = 0$ and $t/\tau_{to} = 1.0$ for R_1, R_3 and R_5.

smaller monotonically. After a long decay at $t/\tau_{to} = 1.0$, PDFs of the local turbulent Mach number still show large portion of flow fields in supersonic state. It means that strong shocklets randomly distribute in flow fields. These random strong discontinuities really pose a great challenge for high-order schemes, which have to well resolve the small scales in smooth regions as well as capture the shock sharply. The PDFs of dilation are presented in Fig 7 as well. At the beginning, all PDFs are symmetric and in a narrow range from -1.08 to 1.08. With the evolving of flows, the systems experience a sharp increase of dilation. The PDFs range approximately from -60 to 20 at $t/\tau_{to} = 1.0$, which means that the strong compression and expansion regions appear in flow fields. All PDFs show strong negative tales, which are the most significant flow structures of isotropic compressible turbulence resulting from the shocklets. In particular, the proportion of negative tail of supersonic isotropic turbulence is larger than that of high subsonic regime, which indicates that shocklets appear in the former case more frequently than that in the latter one. The root-mean-square dilation $\langle\theta\rangle^*$ at $t/\tau_{to} = 1.0$ of these cases are given in Table 3, and it can be concluded that the higher initial turbulent Mach number possess a much higher root-mean-square dilation, i.e. the stronger compressibility effect of isotropic compressible turbulence in supersonic regime. Focusing on physical mechanism of isotropic compressible turbulence, DNS on much higher turbulent Mach number up to $Ma_{t0} = 2.0$ and higher Taylor microscale Reynolds number $Re_{\lambda 0} = 120$ have been obtained by current scheme, which will be presented in the coming paper.

To study the behavior of supersonic isotropic compressible turbulence further, the iso-surfaces of second invariant of velocity gradient tensor $Q = 25$ and contours of normalized dilation $\theta/\langle\theta\rangle^*$

Table 3
Isotropic compressible turbulence with different high turbulent Mach number.

Test	R_0	R_1	R_2	R_3	R_4	R_5
Ma_{t0}	0.5	0.8	0.9	1.0	1.1	1.2
dt_{ini}/τ_0	27.08/1000	22.37/1000	23.73/1000	18.25/1000	18.68/1000	19.02/1000
$\langle\theta\rangle^*$	2.12	3.39	3.87	4.28	4.65	4.90

$\langle\theta\rangle^*$ is the root-mean-square dilation at $t/\tau_{to} = 1.0$

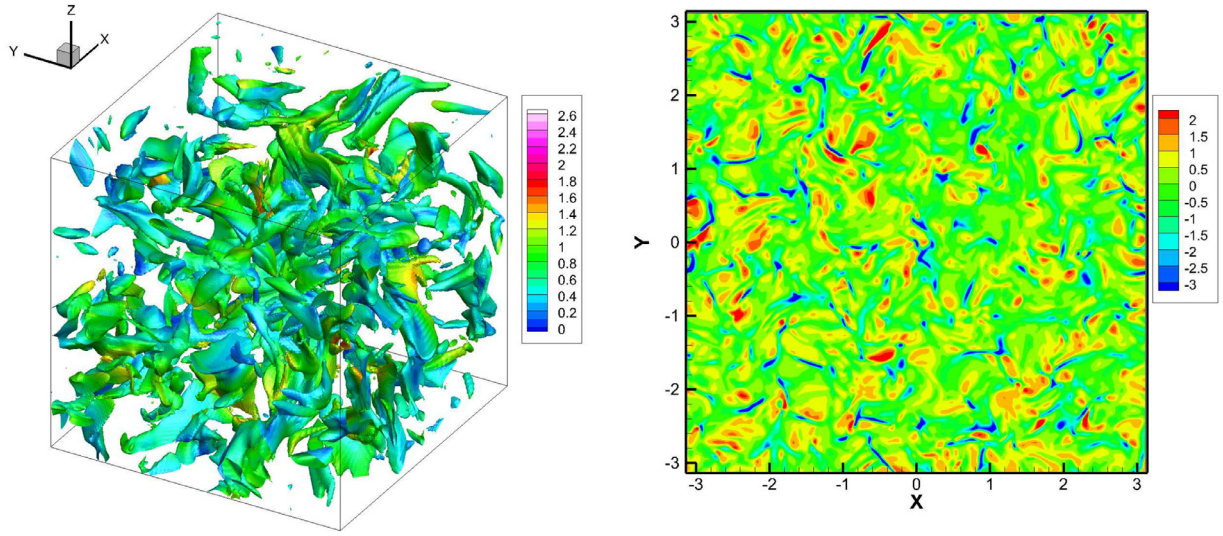

Fig. 8. Iso-surface of the second invariant of velocity gradient tensor $Q = 25$ and contour of normalized dilation $\theta/\langle\theta\rangle^*$ on $z = 0$ slice with $Re_{\lambda 0} = 72$ and $Ma_{t0} = 0.8$ at $t/\tau_{to} = 1.0$.

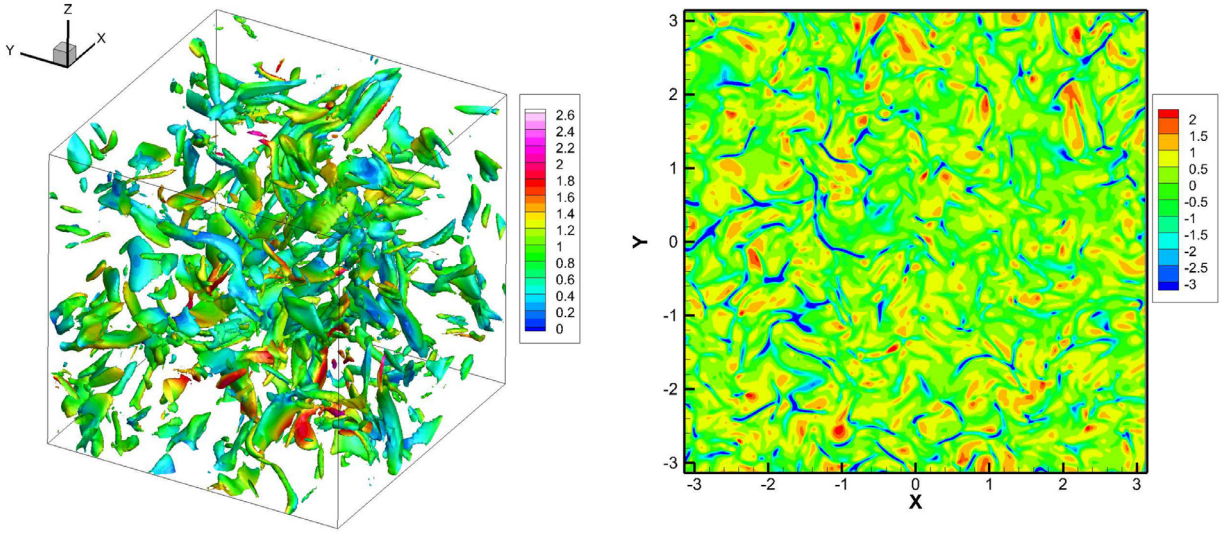

Fig. 9. Iso-surface of the second invariant of velocity gradient tensor $Q = 25$ and contour of normalized dilation $\theta/\langle\theta\rangle^*$ on $z = 0$ slice with $Re_{\lambda 0} = 72$ and $Ma_{t0} = 1.2$ at $t/\tau_{to} = 1.0$.

on $z = 0$ slices with $Ma_{t0} = 0.8$ and $Ma_{t0} = 1.2$ are presented in Figs. 8 and 9, respectively. Iso-surfaces are also colored by the local turbulent Mach number in a 128^3 sub-domain covering $(105\eta_0)^3$, where the sub-domain is located at the center of the whole domain. A quite wide range of vortex structure is presented in flow fields for both cases, and the supersonic isotropic compressible turbulence shows a much higher local turbulent Mach number region than the subsonic one after the same decay. Contours of normalized dilation $\theta/\langle\theta\rangle^*$ shows very different behavior between the compression motion and expansion motion. Strong compression regions $\theta/\langle\theta\rangle^* \leq -3$ are usually recognized as shocklets [9]. In current study, shocklets behave in the shape of narrow and long "ribbon", while high expansion regions $\theta/\langle\theta\rangle^* \geq 2$ are in the type of localized "block". In addition, strong compression regions are close to several regions of high expansion. This behavior is consistent with the physical intuitive that expansion regions can be identified just downstream of shock waves [20]. These random distributed shocklets and high expansion region lead to strong spatial gradient in flow fields. Compared with R_1 in subsonic regime, the supersonic case R_5 contains much more crisp shocklets, which pose much greater challenge for high-order schemes when implementing DNS for isotropic turbulence in supersonic regime. In comparison with previous studies, much higher turbulent Mach number can be simulated by the current scheme, which provide confidence on HGKS for the study of challenging compressible turbulence problems, such as shock-boundary interaction.

Time history of key statistical quantities are presented in Fig. 10, which provides benchmark solution for simulating isotropic compressible turbulence up to supersonic regime. The normalized root-mean-square density ρ_{rms}/Ma_{t0}^2 decreases monotonically with the increase of initial turbulent Mach number. As the initial turbulent Mach number increases, the peak of dissipation increases as well. For incompressible turbulence, the normalized turbulent kinetic energy and ensemble total dissipation rate ε are assumed in universal power decaying rate as $K/K_0 \approx (t/t_0)^{-n}$ and $\varepsilon/\varepsilon_0 \approx (t/t_0)^{-(n+1/n)}$, where n is usually treat as a constant, i.e. $n = 10/7$ based on the Loitsianskii invariant [3], $n = 6/5$ predicted assuming a constant Staffman invariant, and $n = 3/2$ in [56]. However, as in subsonic regime [9], it can be clearly observed that the normalized turbulent kinetic energy and ensemble total dissipation

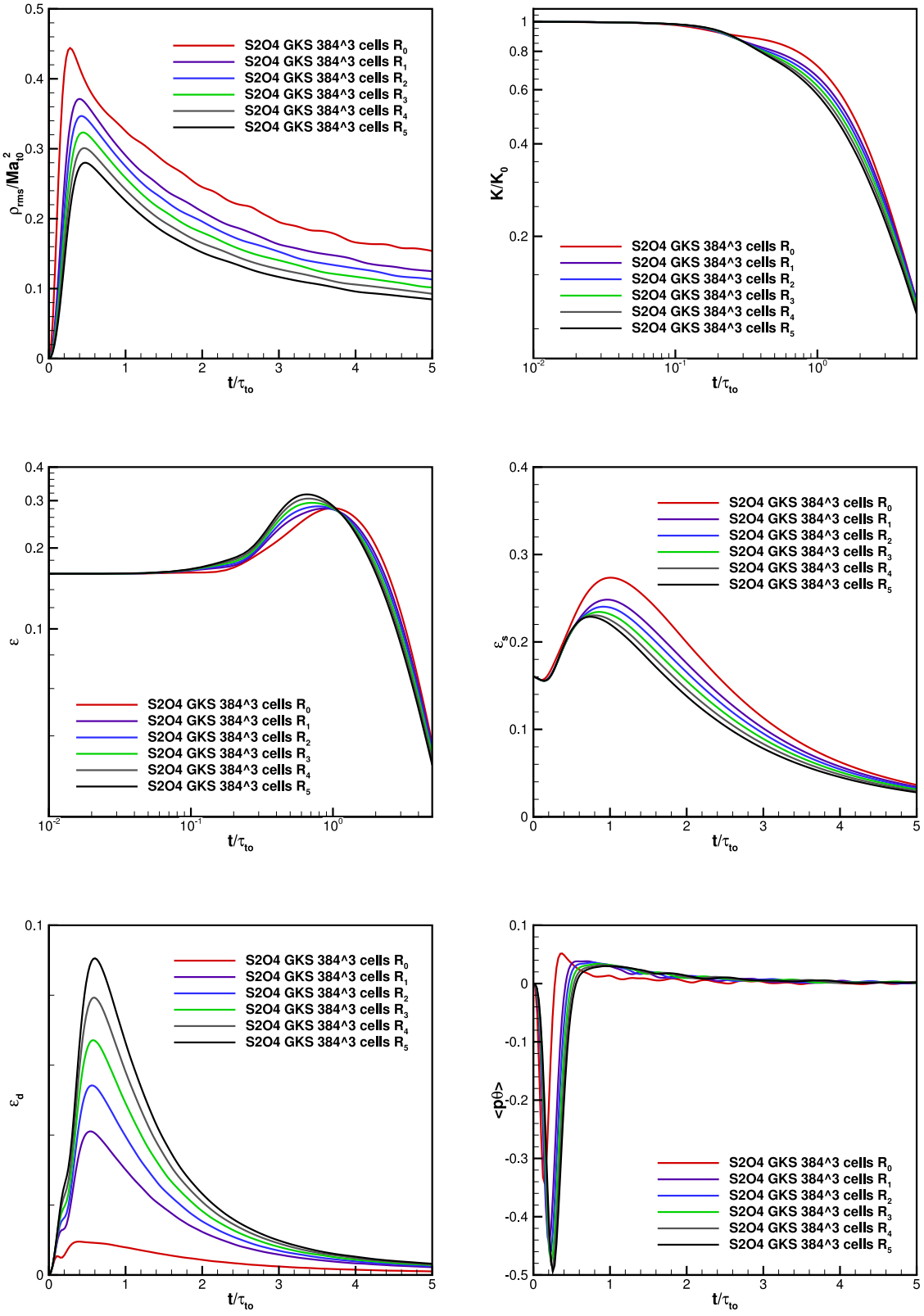

Fig. 10. Time history of ρ_{rms}/Ma_{t0}^2, K/K_0, ε, ε_d, ε_s and $\langle p\theta \rangle$ for cases $R_0 - R_5$.

rate in isotropic compressible turbulence do not show any universal power decaying rate. Obviously, ensemble solenoidal dissipation rate ε_s decreases with the increase of Ma_{t0}, while the dilational dissipation rate ε_d rises with the increase of Ma_{t0}. Remarkably, the peak of ensemble dilational dissipation rate ε_d in supersonic isotropic turbulence $Ma_{t0} = 1.2$ is almost 8 times larger than that of subsonic isotropic turbulence $Ma_{t0} = 0.5$. For solenoidal forced compressible isotropic turbulence, it has been shown that the dilatational dissipation rate of kinetic energy normalized by the solenoidal dissipation rate is proportional to $Ma_t^4 Re_\lambda^{-2} \log Re_\lambda$

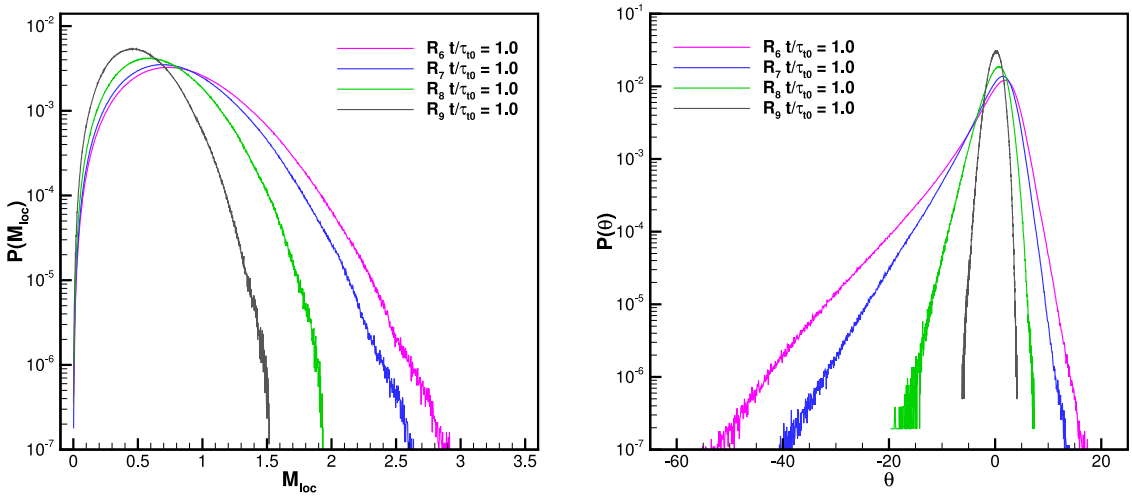

Fig. 11. PDF of local turbulent Mach number and dilation at $t/\tau_{to} = 1.0$ for cases $R_6 - R_9$.

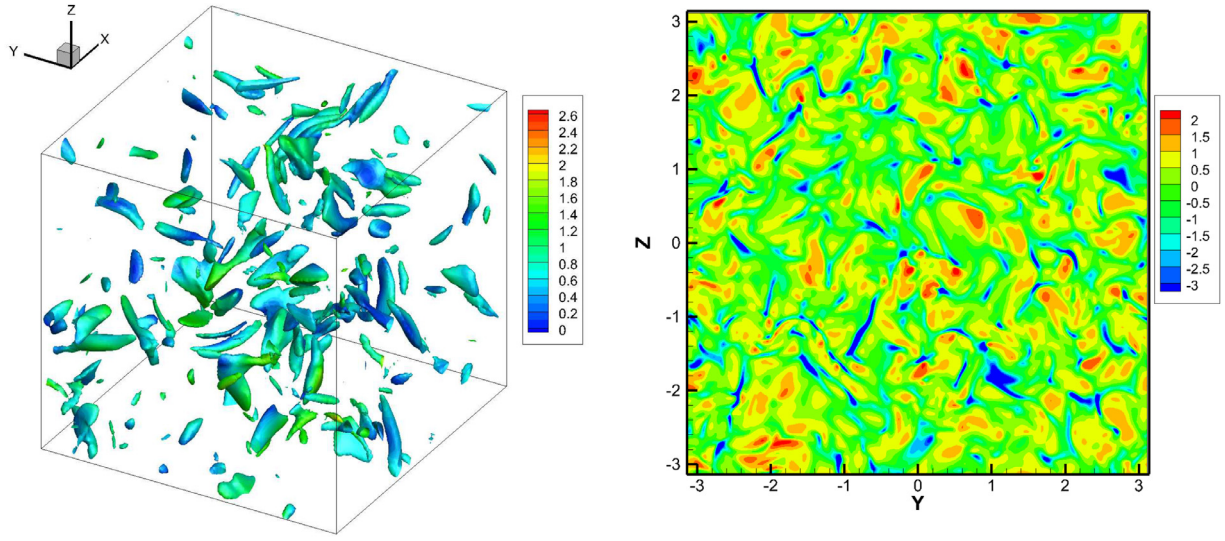

Fig. 12. Iso-surface of the second invariant of velocity gradient tensor $Q = 25$ and contour of normalized dilation $\theta/\langle\theta\rangle^*$ for R_7 on $x = 0$ slice at $t/\tau_{to} = 1.0$.

at small turbulent Mach numbers $Ma_t \leq 0.2$ and is proportional to Ma_t^5 at moderate turbulent Mach numbers $0.4 \leq Ma_t \leq 1.0$ [54]. The dilational dissipation mechanism has not been rarely absorbed in traditional eddy-viscosity LES models [55], and current DNS results provide the first step results for constructing turbulence model in supersonic regime. The time of lowest peak of ensemble pressure-dilation transfer $\langle p\theta \rangle$ becomes larger with the higher initial turbulent Mach number. In addition, $\langle p\theta \rangle$ change signs during the evolution and preserve small but positive thereafter, which agree with earlier study for subsonic isotropic turbulence [51]. It is reported that the ratio between the ensemble pressure-dilation term and the right hand side of Eq. (11) becomes small for solenoidal forced quasi-stationary supersonic isotropic turbulence [21]. However, during the early stage of the decaying supersonic isotropic turbulence, the ensemble pressure-dilation term can be in the same order of ensemble total dissipation rate.

4.3. Taylor microscale Reynolds number effect

In this section, the effect from the Taylor microscale Reynolds number for isotropic compressible turbulence is studied. Power-law decay for incompressible turbulence with low Taylor microscale Reynolds number, i.e. $Re_{\lambda 0} \leq 50$ has been investigated in earlier work [57,58]. The current study focuses on the isotropic turbulence with low Taylor microscale Reynolds number in supersonic regime, and the cases $R_6 - R_9$ with a fixed initial supersonic turbulent Mach number $Ma_{t0} = 1.2$ are listed in Table. 4. The grid size is set to meet the requirement $\kappa_{\max}\eta_0 \geq 2.71$ and all simulations are guided by previous criterion of fourth-order GKS. As shown in Fig. 11, PDFs of local turbulent Mach number still show large portion of supersonic state at $t/\tau_{to} = 1.0$, while the range of PDF decreases with the decreasing of Taylor microscale Reynolds number. Meanwhile, PDFs of dilation presented in Fig. 11 are skewed and the negative tails resulted from the shocklets becomes shorter at the smaller Taylor microscale Reynolds number. Isotropic compressible turbulence at lower Taylor microscale Reynolds number demonstrates a smaller range of dilation, which is consistent with

Table 4
Supersonic isotropic turbulence with different $Re_{\lambda 0}$.

Test	R_6	R_7	R_8	R_9
$Re_{\lambda 0}$	60	40	20	10
Grid size	384^3	384^3	256^3	256^3
$\kappa_{\max}\eta_0$	2.97	3.64	3.43	4.85
dt_{ini}/τ_0	19.03/1000	19.03/1000	23.75/1000	23.75/1000

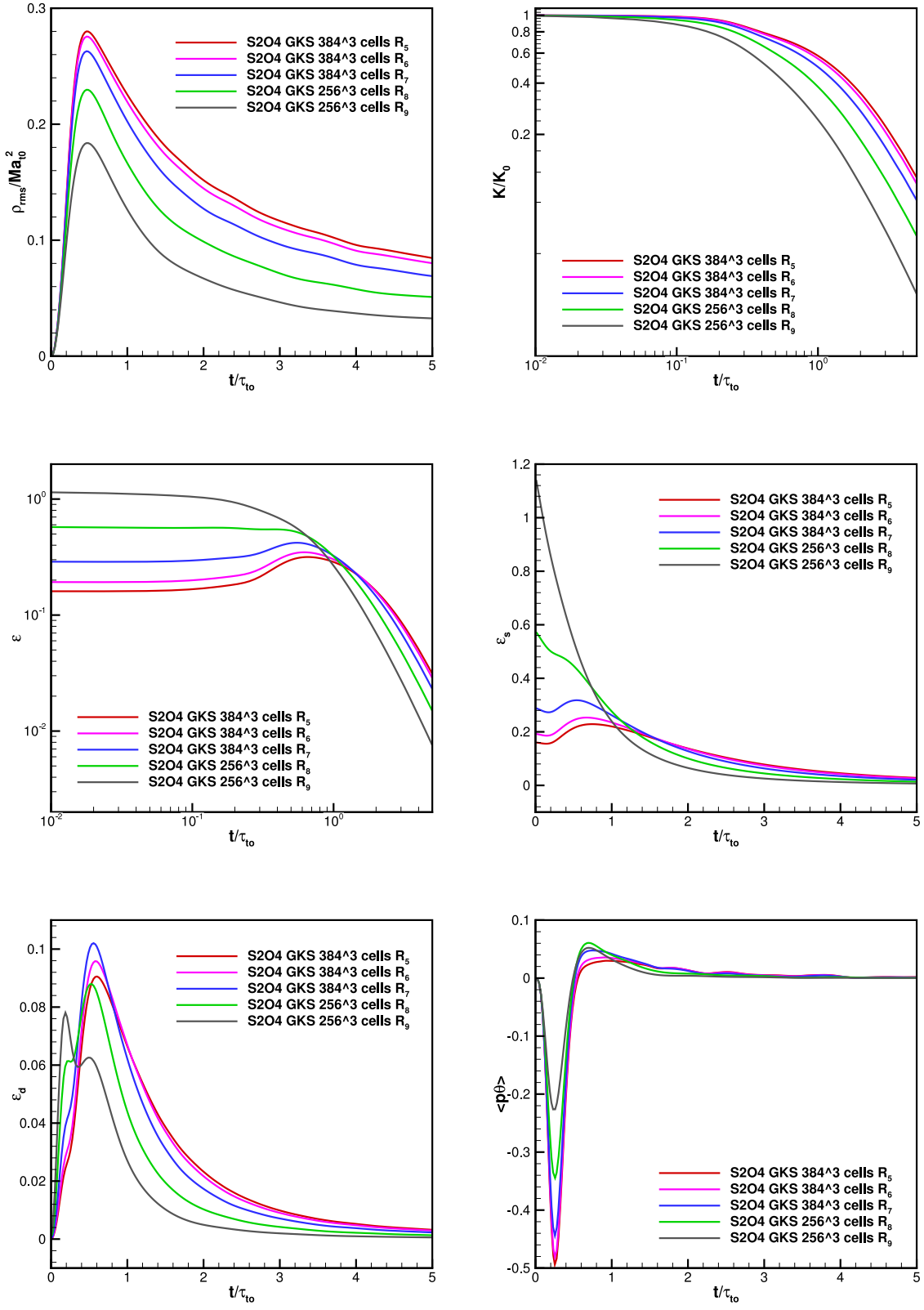

Fig. 13. Time history of ρ_{rms}/Ma_{t0}^2, K/K_0, ε, ε_d, ε_s and $\langle p\theta \rangle$ for cases $R_6 - R_9$.

physical insight that the lower Taylor microscale Reynolds number means the stronger viscous effect, and the stronger dissipation smooths the flow fields and leads to weaker compression regions and expansion regions. Iso-surface of the second invariant of velocity gradient tensor $Q = 25$ and contour of normalized dilation $\theta/\langle\theta\rangle^*$ for R_7 at $x = 0$ slice are presented in Fig. 12, where $\langle\theta\rangle^*$ is root-mean-square dilation at $t/\tau_{to} = 1.0$. Iso-surface is colored by local turbulent Mach number in a 128^3 sub-domain covering $(78\eta_0)^3$, where the sub-domain is located at the center of the full domain. A smaller range of vortex structure in flow fields

is observed in Fig. 12 compared with Fig. 9. Contour of normalized dilation $\theta/\langle\theta\rangle^*$ shows the wider 'ribbon' for strong shocklets and bigger 'block' for high expansion region compared with these from moderate Taylor microscale Reynolds number. This result confirms the fact that the stronger dissipation for the lower Taylor microscale Reynolds number supersonic compressible turbulence smooths the flow fields and makes the transition of compression regions gently.

The key statistical quantities are presented in Fig. 13 which provide benchmark solutions for studying supersonic isotropic turbulence at low Taylor microscale Reynolds number. The normalized root-mean-square density ρ_{rms}/Ma_{t0}^2 decreases with the decrease of initial Taylor microscale Reynold number. The lower Taylor microscale Reynolds number corresponds to higher ensemble total dissipation rate ε during the evolution of this system, which is the direct result from the stronger viscous effect at lower $Re_{\lambda 0}$. It is clear that ensemble solenoidal dissipation rate ε_s decreases with the decrease of $Re_{\lambda 0}$, while the ensemble dilational dissipation rate ε_d seems slightly dependent on $Re_{\lambda 0}$. The behavior of ensemble dilational dissipation rate needs further study in detail, which is pretty meaningful for constructing compressible LES model for supersonic and hypersonic compressible turbulence. In addition, the solenoidal and dilational dissipation rate play the dominant role in hypersonic transition to turbulence reported in previous experiments [59–61]. Current high-order robust scheme will be used to validate and provide more detailed analysis for such hypersonic flows. The moment of lowest peak of ensemble pressure-dilation transfer $\langle p\theta\rangle$ is independent of $Re_{\lambda 0}$ and only depends on Ma_{t0} compared with Fig. 10, while the lowest peak decreases with the decrease of $Re_{\lambda 0}$. Similar with Fig. 10, $\langle p\theta\rangle$ changes signs during the evolution and preserves small but positive value. The similar behavior is observed that the ensemble pressure-dilation term can not be neglected compared with ensemble total dissipation rate in the early stage of evolution, as it has the same order of ensemble total dissipation rate.

5. Conclusions

This paper intends to address the accuracy and robustness of HGKS in DNS for isotropic compressible turbulence simulations up to supersonic regime. Key statistical quantities are compared with high-order compact finite difference scheme to determine the DNS criterion. As a balance between the robustness and accuracy, the WENO-Z reconstruction is properly chosen in the current scheme. The numerical tests show that the minimum spatial resolution parameter $\kappa_{\max}\eta_0 \geq 2.71$ and the maximum temporal resolution parameter $\Delta t_{ini}/\tau_0 \leq 27.08/1000$ for the fourth-order GKS is adequate for resolving the isotropic compressible turbulence. Guided by such a criterion, isotropic compressible turbulence are simulated for turbulent Mach number Ma_{t0} from the nonlinear subsonic regime 0.8 to the supersonic one 1.2, and low Taylor microscale Reynolds number from 10 to 72. A wide range for PDF of local turbulent Mach number, strong random shocklets, and high expansion regions appear with high initial turbulent Mach number. The isotropic turbulence with high turbulent Mach number up to supersonic regime has been studied. The accuracy and robustness of the fourth-order GKS have been fully confirmed. Statistical quantities are provided for these cases, which provide benchmark solutions for supersonic isotropic compressible turbulence. The ensemble budget of the turbulent kinetic energy is analyzed, which plays an important data base in modeling supersonic and hypersonic compressible turbulence. The solenoidal dissipation rate decreases with the increase of both Ma_{t0} and $Re_{\lambda 0}$. Meanwhile, the dilational dissipation rate increases with the increase of Ma_{t0} due to strong compressibility effect, and it seems slightly dependent on $Re_{\lambda 0}$. The HGKS provides a valid tool for studying compressible turbulence. The physics of isotropic compressible turbulence as well as the construction of compressible LES model in supersonic regime will be studied. At the current stage, the DNS on a much higher turbulent Mach number up to $Ma_{t0} = 2.0$ and higher Taylor microscale Reynolds number $Re_{\lambda 0} = 120$ have been obtained by HGKS. All these results and the analysis of physical mechanism of isotropic compressible turbulence will be presented in the subsequent paper.

Acknowledgments

The current research is supported by National Science Foundation of China (11772281, 91852114), Hong Kong Research Grant Council (16206617, 11701038) and the Fundamental Research Funds for the Central Universities. The authors would like to thank TianHe-II in Guangzhou for providing high performance computational resources.

References

[1] Aluie H. Compressible turbulence: the cascade and its locality. Phys Rev Lett 2011;106:174502.
[2] Lele SK. Compressibility effects on turbulence. Annu Rev Fluid Mech 1994;26:211–54.
[3] Sagaut P, Cambon C. Homogeneous turbulence dynamics. Springer; 2008.
[4] Wang LP, Chen SY, Brasseur JG, Wyngaard JC. Examination of hypotheses in the Kolmogorov refined turbulence theory through high-resolution simulations. Part 1. Velocity field. J Fluid Mech 1996;309:113–56.
[5] Moin P, Mahesh K. Direct numerical simulation: a tool in turbulence research. Annu Rev Fluid Mech 1998;30:539–78.
[6] Chen SY, Doolen GD. Lattice Boltzmann method for fluid flows. Annu Rev Fluid Mech 1998;30:329–64.
[7] Yu HD, Girimaji SS, Luo LS. Lattice Boltzmann simulations of decaying homogeneous isotropic turbulence. Phys Rev E 2005;71:016708.
[8] Lele SK. Compact finite difference schemes with spectral-like resolution. J Comput Phys 1992;103:16–42.
[9] Samtaney R, Pullin DI, Kosović B. Direct numerical simulation of decaying compressible turbulence and shocklet statistics. Phys Fluids 2001;13:1415–30.
[10] Pirozzoli S, Grasso F. Direct numerical simulations of isotropic compressible turbulence: influence of compressibility on dynamics and structures. Phys Fluids 2004;16:4386–407.
[11] Jagannathan S, Donzis DA. Reynolds and mach number scaling in solenoidally-forced compressible turbulence using high-resolution direct numerical simulations. J Fluid Mech 2016;789:669–707.
[12] Porter DH, Pouquet A, Woodward PR. A numerical study of supersonic turbulence. Theor Comput Fluid Dyn 1992;4:13–49.
[13] Porter DH, Pouquet A, Woodward PR. Kolmogorov-like spectra in decaying three-dimensional supersonic flows. Phys Fluids 1994;6:2133–42.
[14] Adams NA, Shariff K. A high-resolution hybrid compact-ENO scheme for shock-turbulence interaction problems. J Comput Phys 1996;127:27–51.
[15] Wang JC, Wang LP, Xiao ZL, Shi Y, Chen SY. A hybrid numerical simulation of isotropic compressible turbulence. J Comput Phys 2010;229:5257–79.
[16] Liu LQ, Wang JC, Shi Y, Chen SY, He XT. A hybrid numerical simulation of supersonic isotropic turbulence. Comm Comput Phys 2019;25:189–217.
[17] Wang JC, Wang LP, Xiao ZL, He XT, Chen SY. Scaling and statistics in three-dimensional compressible turbulence. Phys Rev Lett 2012;108:214505.
[18] Wang JC, Gotoh T, Watanabe T. Scaling and intermittency in compressible isotropic turbulence. Phys Rev Fluids 2017;2:053401.
[19] Wang JC, Gotoh T, Watanabe T. Shocklet statistics in compressible isotropic turbulence. Phys Rev Fluids 2017;2:023401.
[20] Wang JC, Wan MP, Chen S, Xie CY, Chen SY. Effect of shock waves on the statistics and scaling in compressible isotropic turbulence. Phys Rev E 2018;97:043108.
[21] Wang JC, Wan MP, Chen S, Chen SY. Kinetic energy transfer in compressible isotropic turbulence. J Fluid Mech 2018;841:581–613.
[22] Bhatnagar PL, Gross EP, Krook M. A model for collision processes in gases i: small amplitude processes in charged and neutral one-component systems. Phys Rev 1954;94:511–25.
[23] Chapman S, Cowling TG. The mathematical theory of non-uniform gases. 3rd ed. Cambridge University Press; 1990.
[24] Xu K. Gas kinetic schemes for unsteady compressible flow simulations. Lecure Note Ser. 1998-03, Von Karman Institute for Fluid Dynamics Lecture; 1998.
[25] Xu K. A gas-kinetic BGK scheme for the Navier–Stokes equations and its connection with artificial dissipation and Godunov method. J Comput Phys 2001;171:289–335.
[26] Xu K. Direct modeling for computational fluid dynamics: construction and application of unified gas kinetic schemes. World Scientific; 2015.
[27] Li QB, Xu K, Fu S. A high-order gas-kinetic Navier–Stokes flow solver. J Comput Phys 2010;229:6715–31.
[28] Luo J, Xu K. A high-order multidimensional gas-kinetic scheme for hydrodynamic equations. Sci China Technol Sci 2013;56:2370–84.

[29] Li J, Du Z. A two-stage fourth order time-accurate discretization for Lax–Wendroff type flow solvers i. Hyperbolic conservation laws. SIAM J Sci Comput 2016;38:3046–69.
[30] Pan L, Xu K, Li QB, Li JQ. An efficient and accurate two-stage fourth-order gas-kinetic scheme for the Navier–Stokes equations. J Comput Phys 2016;326:197–221.
[31] Zhao FX, Ji X, Shyy W, Xu K. Compact higher-order gas-kinetic schemes with spectral-like resolution for compressible flow simulations. Adv Aerodyn 2019;1:13.
[32] Pan L, Li JQ, Xu K. A few benchmark test cases for higher-order euler solvers. Numer Math 2017;10:711–36.
[33] Ji X, Zhao FX, Shyy W, Xu K. A family of high-order gas-kinetic schemes and its comparison with Riemann solver based high-order methods. J Comput Phys 2018;356:150–73.
[34] Cao GY, Liu HL, Xu K. Physical modeling and numerical studies of three-dimensional non-equilibrium multi-temperature flows. Phys Fluids 2018;30:126104.
[35] Jiang J, Qian YH. Implicit gas-kinetic BGK scheme with multigrid for 3D stationary transonic high-Reynolds number flows. Comput Fluids 2012;66:21–8.
[36] Righi M. A gas-kinetic scheme for turbulent flow, flow. Turbul Combust 2016;97:121–39.
[37] Tan S, Li QB, Xiao ZX, Fu S. Gas kinetic scheme for turbulence simulation. Aerosp Sci Technol 2018;78:214–27.
[38] Cao G.Y., Su H.M., Xu J.X., Xu K.. Implicit high-order gas kinetic scheme for turbulence simulation. 2018b. arXiv:1811.08005.
[39] Liao W, Peng Y, Luo LS. Gas-kinetic schemes for direct numerical simulations of compressible homogeneous turbulence. Phys Rev E 2009;80:046702.
[40] Kumar G, Girimaji SS, Kerimo J. WENO-enhanced gas-kinetic scheme for direct simulations of compressible transition and turbulence. J Comput Phys 2013;234:499–523.
[41] Liu XD, Osher S, Chan T. Weighted essentially non-oscillatory schemes. J Comput Phys 1994;115:200–12.
[42] Jiang GS, Shu CW. Efficient implementation of weighted ENO schemes. J Comput Phys 1996;126:202–28.
[43] Castro M, Costa B, Don WS. High order weighted essentially non-oscillatory WENO-z schemes for hyperbolic conservation laws. J Comput Phys 2011;230:1766–92.
[44] Pan L, Xu K. Two-stage fourth-order gas-kinetic scheme for three-dimensional euler and Navier–Stokes solutions. Int J Comput Fluid Dyn 2018;32:395–411.
[45] Kida S, Orszag SA. Energy and spectral dynamics in forced compressible turbulence. J Sci Comput 1990;5:85–125.
[46] Kida S, Orszag SA. Enstrophy budget in decaying compressible turbulence. J Sci Comput 1990;5:1–34.
[47] Passot T, Pouquet A. Numerical simulation of compressible homogeneous flows in the turbulent regime. J Fluid Mech 1987;181:441–66.
[48] Yoshizawa A, Horiuti K. A statistically-derived subgrid-scale kinetic energy model for the large-eddy simulation of turbulent flows. J Phys SocJpn 1985;54:2834–9.
[49] Pope S.B.. Turbulent flows, cambridge. 2001.
[50] Chai XC, Mahesh K. Dynamic-equation model for large-eddy simulation of compressible flows. J Fluid Mech 2012;699:385–413.
[51] Sarkar S, Erlebacher G, Hussaini MY, Kreiss HO. The analysis and modelling of dilatational terms in compressible turbulence. J Fluid Mech 1991;227:473–493.
[52] Wang P, Wang LP, Guo ZL. Comparison of the lattice Boltzmann equation and discrete unified gas-kinetic scheme methods for direct numerical simulation of decaying turbulent flows. Phys Rev E 2016;94:043304.
[53] Eswaran V, Pope SB. An examination of forcing in direct numerical simulations of turbulence. Comput Fluids 1988;16:257–78.
[54] Wang JC, Gotoh T, Watanabe T. Spectra and statistics in compressible isotropic turbulence. Phys Rev Fluids 2017;2:013403.
[55] Chai XC, Wang JC, Li H, Wan MP, Chen SY. A modified optimal LES model for highly compressible isotropic turbulence. Phys Fluids 2018;30:065108.
[56] Saffman PG. The large-scale structure of homogeneous turbulence. J Fluid Mech 1967;27:581–93.
[57] Huang MJ, Leonard A. Power-law decay of homogeneous turbulence at low Reynolds numbers. Phys Fluids 1994;6:3765–75.
[58] Mansour NN, Wray AA. Decay of isotropic turbulence at low Reynolds number. Phys Fluids 1994;6:808–14.
[59] Lee CB, Wu JZ. Transition in wall-bounded flows. Appl Mech Rev 2008;61:030802.
[60] Zhu YD, Zhang CH, Chen X, Yuan H, Wu JZ, Chen SY, Lee CB, Gad-el Hak M. Transition in hypersonic boundary layers: role of dilatational waves. AIAA J 2016;54:3039–49.
[61] Zhu YD, Chen X, Wu JZ, Chen SY, Lee CB, Gad-el Hak M. Aerodynamic heating in transitional hypersonic boundary layers: role of second-mode instability. Phys Fluids 2018;30:011701.